Advances in Aircraft and Spacecraft Science, *Vol. 9, No. 5 (2022) 401-414*
https://doi.org/10.12989/aas.2022.9.5.401

Optimal battery selection for hybrid rocket engine

Filippo Masseni*

Dipartimento di Ingegneria Meccanica ed Aerospaziale, Politecnico di Torino, Corso Duca degli Abruzzi 24, Torino, Italy

(Received November 25, 2021, Revised June 16, 2022, Accepted July 5, 2022)

Abstract. In the present paper, the optimal selection of batteries for an electric pump-fed hybrid rocket engine is analyzed. A two-stage Mars Ascent Vehicle, suitable for the Mars Sample Return Mission, is considered as test case. A single engine is employed in the second stage, whereas the first stage uses a cluster of two engines. The initial mass of the launcher is equal to 500 kg and the same hybrid rocket engine is considered for both stages. Ragone plot-based correlations are embedded in the optimization process in order to chose the optimal values of specific energy and specific power, which minimize the battery mass ad hoc for the optimized engine design and ascent trajectory. Results show that a payload close to 100 kg is achievable considering the current commercial battery technology.

Keywords: electric turbo-pump; hybrid rocket engines; multidisciplinary optimization; trajectory optimization

1. Introduction

Hybrid Rocket Engines (HREs) are a promising propulsion system which gathers positive features from heritage ones. HREs are affordable and simple like solid rocket motors (SRMs), while their performance and control capabilities are close to semi-crio and storable liquid rocket engines (LREs). Furthermore, the environmental impact of hybrids is lower with respect to SRMs, which emit large amount of chlorine compounds. For these reasons, many research groups all around the world are currently focusing on the analysis of hybrids, from both the numerical and experimental point of view (Nagata *et al*. 2014, Saito *et al*. 2017, Funami 2019).

In the last decades, at the Politecnico di Torino the research activities focused on the design and optimization of hybrid rocket engines for several applications (Casalino and Pastrone 2010a, Casalino and Pastrone 2012, Casalino *et al*. 2019o, Casalino *et al*. 2021a, Casalino *et al*. 2021b), among them hybrid-powered Mars Ascent Vehicle (MAV) concepts in the context of a Sample Return Mission (Casalino and Pastrone 2014). In this context, the hybrid engine proved to be a viable alternative to other propulsion system options (McCollum *et al*. 2019, Oglesby *et al*. 2019, Evans and Cantwell 2019, Muirhead and Karp 2019). In such specific application, the use of a solid fuel and a liquid oxidizer grants many intriguing features, such as high safety, throttle-ability, shut-down/restart capabilities, and less issues related to Mars' harsh environment. Moreover, Liquid OXygen (LOX) can be produced in-situ from Mars' atmosphere, and may be used as

*Corresponding author, Assistant Professor, E-mail: filippo.masseni@polito.it

Copyright © 2022 Techno-Press, Ltd.
http://www.techno-press.org/?journal=aas&subpage=7 ISSN: 2287-528X (Print), 2287-5271 (Online)

oxidizer for the HRE analogous to the most common liquid rocket engine-based concepts (Boiron and Cantwell 2013, Shotwell *et al*. 2016). Concerning the fuel choice, paraffin-based wax is considered, as the most viable way to mitigate the low regression rate issue typical of hybrids (Karabeyoglu *et al*. 2002).

On the other hand, the unique combustion process of HREs and their peculiar control feature, only the liquid propellant flow can be controlled, make it necessary to perform a coupled optimization of engine and trajectory. This process is here carried out by means of a hybrid optimization procedure, which takes advantage of an indirect method for the trajectory optimization combined with a direct method for the engine design optimization (Casalino and Pastrone 2005a).

In previous works on the same topic, different feed system options and launcher configurations have been considered and their performance compared (Casalino and Pastrone 2014, Casalino *et al*. 2021c). In general, the use of an electrically driven turbo-pump feed system results in remarkable payload mass capability with respect to more conventional gas pressurized feed systems (Casalino and Pastrone 2010b, Casalino *et al*. 2019). In this context, the selection of the battery plays a major role, because its electrical properties affect the propulsion system dry mass. Lithium batteries are well suited for aerospace applications due to their compact size and high specific performance.

In the present work, three properties of the batteries are analyzed, namely specific energy, specific power and their ratio, which is commonly called characteristic time. Obviously, higher specific properties result in lighter battery and smaller engine dry mass (i.e., larger payload mass). However, from this point of view, lithium batteries are characterized by quite wide ranges for the specific properties: from high energy/low power batteries to very high power/low energy batteries. Thus, in this paper an early design tool for the selection of the most suitable battery for a specific HREs mission is proposed and applied to the MAV test case.

2. Engine design and optimization

In the present work, liquid oxygen and paraffin-based wax are considered as propellants due to the large regression rate value delivered, which enables a single port grain design, and the possibility to obtain the oxidizer from Mars' atmosphere.

The performance of the propellants combination are evaluated by means of NASA CEA code (rocket mode) (McBride *et al*. 1994), assuming a constant chamber pressure $p_c = 10$ bar, variable mixture ratio α, 100wt% paraffin as fuel, and 100wt% O2(L) as oxidizer. The error introduced by the constant pressure assumption is small for the mixture ratio and pressure ranges of variation of the present work. In the nozzle, an ideal frozen equilibrium expansion (i.e., an isentropic expansion without changes in the chemical composition of the gas mixture) is employed in order to evaluate the characteristic velocity c^*. In addition, the author introduces a c^*-efficiency equal to 0.96, which takes into account the well-known low combustion efficiency of hybrids (Sutton and Biblarz, 2001). The actual values of characteristic velocity c^* and specific heat ratio γ depend on the mixture ratio α, thus third-degree polynomial curves fittings of $c^* = c^*(\alpha)$ and $\gamma = \gamma(\alpha)$ are embedded in the numerical procedure. The thrust coefficient C_F can be evaluated from nozzle expansion area ratio E and ambient pressure p_0, assuming constant γ, an isentropic expansion and a 0.98 C_F-efficiency, introduced to account for losses (Sutton and Biblarz 2001)

$$C_F = 0.98\left\{\sqrt{\frac{2\gamma^2}{\gamma-1}\left(\frac{2}{\gamma+1}\right)^{\frac{\gamma+1}{\gamma-1}}\left[1-\left(\frac{p_e}{p_c}\right)^{\frac{\gamma-1}{\gamma}}\right]}+E\frac{p_e}{p_c}\right\}-E\frac{p_0}{p_c} \tag{1}$$

The chosen propellants combination allows for a cylindrical grain with a single circular port, thanks to its relatively high regression rate. The author assumes uniform regression rate along the port axis, which is given by the time derivative of the port radius *R*

$$\frac{\mathrm{d}R}{\mathrm{d}t} = a\left(\frac{\dot{m}_O}{A_p}\right)^n \propto \dot{m}_O^n \; R^{-2n} \tag{2}$$

where the regression rate correlation coefficient $a = 9.1 \cdot 10^{-5}$ and exponent $n = 0.69$, when SI units are used (Karabeyoglu *et al*. 2002). In this context, the contribution to overall rocket performance of the combustion of the grain lateral ends is neglected. Pressure losses in the combustion chamber are evaluated by means of an approximate relation, similar to that proposed by Barrere *et al*. for side-burning grains (Barrere *et al*. 1960), which relates the chamber head-end pressure p_1 to the chamber/nozzle stagnation pressure p_c

$$p_1 = \left[1 + 0.2\left(\frac{A_{th}}{A_p}\right)^2\right] p_c \tag{3}$$

The oxidizer flow rate $\dot{m}_O$ during operation is provided by Eq. (4), assuming constant hydraulic resistance (i.e., $Z = \text{constant}$) and incompressible turbulent flow in the oxidizer flow path from the tank to the combustion chamber. The fuel mass flow rate $\dot{m}_F$ and the mixture ratio α are given by Eq. (5) and Eq. (6), respectively.

$$\dot{m}_O = \sqrt{(p_d - p_1)/Z} \tag{4}$$

$$\dot{m}_F = \rho_F A_b \frac{\mathrm{d}R}{\mathrm{d}t} \propto \dot{m}_O^n \; R^{1-2n} \tag{5}$$

$$\alpha = \frac{\dot{m}_O}{\dot{m}_F} \propto \dot{m}_O^{1-n} \; R^{2n-1} \tag{6}$$

The chamber/nozzle stagnation pressure p_c is determined as

$$p_c = \frac{(\dot{m}_O + \dot{m}_F)c^*}{A_{th}} \tag{7}$$

where an isentropic expansion is assumed.

In the proposed model, the engine design is given by four parameters: initial thrust F_i, initial discharge pressure $(p_d)_i$, initial mixture ratio α_i and nozzle expansion area ratio E. The initial discharge pressure $(p_d)_i$ is assumed to fix the initial chamber pressure to $(p_c)_i = 0.4(p_d)_i$. During operation, the ratio p_d/p_c varies, but the aforementioned assumption is able to grant $p_d/p_c > 1.5$ for the whole engine burn, which avoids the coupling between the engine and the oxidizer feed system. The initial port to throat area ratio *J* is fixed and equal to 0.5, in order to limit pressure losses and nonuniform regression, although larger values could grant better performance. The optimal solutions tend to have very high initial thrust levels, resulting in excessive longitudinal accelerations (Price *et al*. 2000). For this reason, F_i has been dropped from the set of engine design variables and the vacuum thrust of each HRE is here fixed to 2.5 kN.

The engine design and initial grain geometry and performance are thus determined from $(p_d)_i$,

α_i and E. The initial value of c^* and γ are given by α_i at engine ignition and E determines p_e/p_c, which in turn allows the computation of C_F and $c = c^* C_F$ knowing the ambient pressure p_0. The propellant mass flow rate at ignition is then

$$(\dot{m}_p)_i = \frac{F_i}{c_i^*(C_F)_i} = (1 + \alpha_i)(\dot{m}_F)_i = \frac{1+\alpha_i}{\alpha_i}(\dot{m}_O)_i \tag{8}$$

At this point, the throat area A_{th} can be calculated by means of Eq. (7). In the present work, nozzle throat erosion effects are neglected, which means that $A_{th} = \text{constant}$ and $E = \text{constant}$ during engine operation. However, the effects of the reduction of nozzle expansion area ratio ϵ due to erosion are the decrease of characteristic velocity c^* and chamber pressure p_c, which can results in slightly lower overall performance of the hybrid propulsion system (Casalino *et al*. 2012, Kamps *et al*. 2021).

The initial port area $(A_p)_i$ is then

$$(A_p)_i = \pi R_i^2 = A_{th}/J \tag{9}$$

whereas the initial burning area $(A_b)_i$ can be computed by means of Eq. (5). In the end, the grain length L_b is obtained by Eq. (10), completely specifying the initial grain geometry.

$$L_b = (A_b)_i/(2\pi R_i) \tag{10}$$

The feed system consists of an electric motor, powered by a battery pack, which drives the turbo-pump feeding the liquid oxidizer into the combustion chamber. The system is assumed to operate at a constant power level, that is determined by the initial values of discharge pressure $p_d = (p_d)_i$ and oxidizer flow rate $\dot{m}_O = (\dot{m}_O)_i$

$$P_e = \frac{\dot{m}_O(p_d - p_t)}{\rho_O \eta_{ep}} = \text{constant} \tag{11}$$

where $\eta_{ep} = 0.53$ is the overall efficiency of the conversion process of electrical energy into flow head rise and ρ_O is the oxidizer density (Kwak *et al*. 2018). A constant 1-bar tank pressure p_t is here considered and the small amount of pressurizing gas mass required to keep it constant during engine operation is neglected. The electric motor and pump mass m_{ep} is then computed as

$$m_{ep} = \frac{P_e}{\delta_{ep}} \tag{12}$$

where $\delta_{ep} = 3.92\ \text{kWkg}^{-1}$ is assumed (Kwak *et al*. 2018). The electric energy required to perform the mission E_e can be easily computed, due to the constant power assumption, as

$$E_e = P_e t_b \tag{13}$$

where t_b is the hybrid rocket engine burning time. At this point, the battery mass can be computed by means of the following equation

$$m_b = 1.2\max\left(\frac{P_e}{\delta_{bp}}, \frac{E_e}{\delta_{be}}\right) = 1.2\,\frac{P_e}{\delta_{bp}}\max\left(1, \frac{t_b}{t^*}\right) \tag{14}$$

where δ_{bp} and δ_{be} are the specific power and energy of the battery. Moreover, the characteristic battery time $t^* = \delta_{be}/\delta_{bp}$ has been introduced, alongside with a 1.2 safety factor. Battery mass is constrained by the most stringent requirement between the power required P_e and energy required E_e. Looking at Eq. (14), one can notice that the battery mass m_b is minimized when $t_b = t^*$, i.e., when the engine burn duration matches the characteristic battery time. However, the actual engine

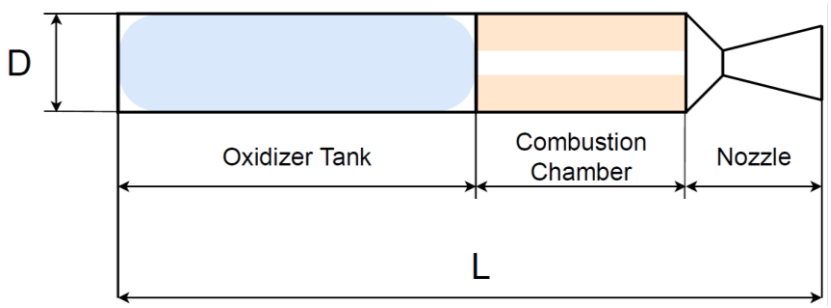

Fig. 1 Mock-up of a single hybrid rocket engine employed in the proposed MAV

burn duration t_b is not known until the optimized ascent trajectory is computed, which, on the other hand, depends on the choice of δ_{be} and δ_{bp} for the battery (i.e., depends on t^*), because they determine the stages dry masses. Thus, two simple correlation, based on Ragone plot for common commercial lithium batteries, are used to express t^* and δ_{be} as functions of δ_{bp} (Budde-Meiwes *et al*. 2013)

$$t^* = 2.237 \cdot 10^6 \delta_{bp}^{-1.21} - 19.01 \tag{15}$$

$$\delta_{be} = -1069 \delta_{bp}^{0.02843} + 1440 \tag{16}$$

These relations are embedded in the trajectory optimization process in order to solve at each iteration the non linear equation $t_b = t^*$ for δ_{bp} (by means of Eq. (15)) and then compute the corresponding δ_{be} (by means of Eq. (16)). In this way, the battery mass can be computed during the ascent trajectory, according to the optimal values of the specific quantities, i.e., such that it is minimized in accordance with Eq. (14).

The numerical integration of Eq. (2) and Eq. (4) gives the solid fuel geometry and oxidizer exhausted mass throughout engine operation. The regression rate, the propellant flow rates (and their ratio α), p_c and p_1 are determined numerically solving Eqs. (2)-(7) and using the fitting for c^* as a function of α. The thrust level is calculated as $F = p_c A_{th} C_F$, once the thrust coefficient C_F has been evaluated at the actual rocket altitude, allowing for trajectory integration. The ambient conditions of Mars' atmosphere as functions of rocket altitude are provided by Eq. (21) and Eq. (22) (see Section 3). Web thickness w and grain outer radius $R_f = R_i + w$ can be computed at engine burnout. At this point, the overall oxidizer and fuel masses are known and the structural masses can be estimated, in order to obtain the launcher payload mass value, which is the optimization merit function to be maximized in the present approach.

The sum of the lengths of oxidizer tank, fuel grain and nozzle gives the engine and stage length. Each stage is encapsulated in a 1-mm thick cylindrical aluminum casing, whose diameter is given by the tank diameter, that is also equal to combustion chamber diameter. A 6-mm insulating liner, whose density is equal to the solid fuel one, is taken into account in the combustion chamber, alongside with an aluminum alloy cylindrical wall. Aluminum is also employed for the cylindrical oxidizer tank. Chamber and tank wall thicknesses are calculated in order to withstand the internal pressures during operation, assuming a 1.25 safety factor and a lower limit of 0.5 mm. A simple mock-up of the hybrid rocket engine configuration is shown in Fig. 1. A 45-deg convergent and a 20-deg divergent nozzle is taken into consideration, together with a phenolic silica ablative layer of uniform thickness, evaluated according to Ref. (Barker *et al*. 1965). The nozzle structural mass

has been neglected due to its small magnitude with respect to the ablative layer mass, which, in addition, has been estimated in a conservative way. In the end, the masses of interstage adapters, separation mechanism, avionics, sensors and thermal control system have been neglected in the present analysis.

The engine design parameters are optimized by means of a direct method, once a set of initial tentative values is provided (Casalino and Pastrone 2005b). An indirect procedure evaluates, in few seconds on a modern personal computer, the optimal trajectory and the corresponding payload mass. Then, the initial tentative values for the engine design parameters are varied by small quantities and the derivatives of the performance index are evaluated with respect to the design parameters. At this point, a numerical procedure based on Newton-Raphson's method is used, in order to compute the set of design parameters which nullify all the partial derivatives of the performance index. The whole procedure requires only a few minutes to obtain the optimal design and the corresponding optimized ascent trajectory, once an initial solution is provided.

3. Rocket configurations and trajectory optimization

In this analysis, the proposed MAV consists of two stages: two hybrid engines are employed in the first stage, whereas a single engine powers the second stage. In the present approach the three HREs are regarded as identical, allowing for the reduction of the development costs of the hybrid propulsion system, with respect to the use of different engines in each stage.

The ascent trajectory is divided into four phases: 1) vertical ascent (followed by an instantaneous velocity rotation), 2) zero-lift gravity-turn ascent until the first stage is exhausted and jettisoned, 3) coast arc and 4) second stage burn with optimal thrust direction until insertion into the desired orbit. The optimization merit function is the MAV payload mass μ, which is given by the second stage final mass minus its dry mass. The j-th phase starts at time t_{j-1} and ends at t_j. A point-mass rocket is considered in order to model the launcher and the state equations are written in an inertial Mars-centered reference frame

$$\frac{\mathrm{d}r}{\mathrm{d}t} = v \quad \frac{\mathrm{d}v}{\mathrm{d}t} = -GM_{\sigma}\frac{r}{|r|^3} + \frac{F-D}{m} \quad \frac{\mathrm{d}m}{\mathrm{d}t} = -\frac{F}{c} \tag{17}$$

Such system of equations is coded in non-dimensional form in the optimization procedure, aiming at the improvement of the numerical accuracy. An inverse-square gravity field is here assumed and the aerodynamic drag is given by

$$D = (1/2)\rho_{atm} C_D S\, v_{rel}^2 \tag{18}$$

where the dependency between the payload mass and the aerodynamic drag is neglected. The cross section S of each sub-rocket is computed as

$$S = N\pi d^2/4 \tag{19}$$

where N is the number of hybrid engines, d is the rocket diameter and the aerodynamic drag coefficient C_D is calculated as a function of the Mach number as reported in Fig. 2. However, it is worth noting that the influence of the aerodynamic drag on the launcher performance is practically negligible because of Mars thin atmosphere.

The rocket relative velocity is computed as v_{rel}=v-ω × r, where ω is Mars's angular velocity. The thrust F can be evaluated as

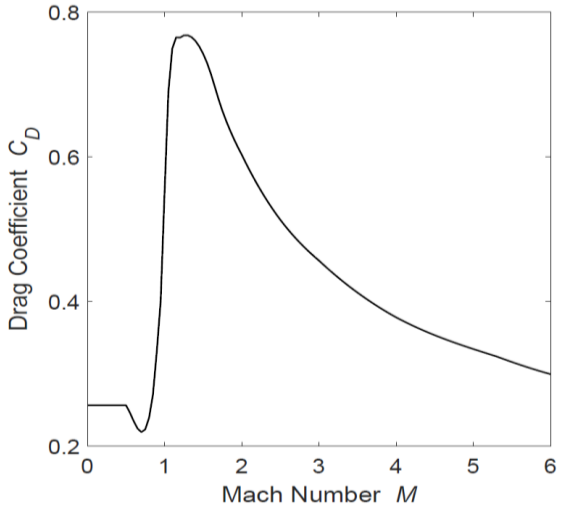

Fig. 2 Drag coefficient

$$F = F_{vac} - EA_{th}p_{atm} \tag{20}$$

where F_{vac} is the engine vacuum thrust, which is a known function of time, once the engine design is given by the design parameters. The values of ambient density ρ_{atm} and pressure p_{atm} as function of rocket altitude h are required for the evaluation of aerodynamic drag D and thrust F. In this analysis, numerical fits of pressure and temperature of Mars atmosphere are used and reported in Eq. (21) and Eq. (22), where SI units (K, Pa, and m) are employed.

$$T = \begin{cases} 242.15 - .000998h, & when\ h \leq 7000\ m \\ 249.75 - .00222h, & when\ h > 7000\ m \end{cases} \tag{21}$$

$$p = 699\mathrm{e}xp(-0.00009h) \tag{22}$$

The atmospheric density ρ_{atm} can be calculated by means of the perfect gas equation ($R = 192.1$ J/kg/K).

The boundary conditions of the problem impose the initial values of the state variables (position, velocity and rocket mass) at $t_0 = 0$ and the altitude at the end of the vertical ascent phase. On the other hand, a circular orbit of given altitude is prescribed at the final time t_f. The use of identical engines in both stages adds a further condition, i.e., $t_4 - t_3 = t_2 - t_0$, because the burning times of the stages have to be equal.

Once the engine design and its performance are given, the Optimal Control Theory (OCT) gives the optimal trajectory. Adjoint variables are associated to the state equations and the Hamiltonian, whose formulation depends on the phase of flight, is

$$H = \lambda_r v + \lambda_v \left(\frac{r}{|r|^3} + \frac{F-D}{m}\right) - \lambda_m \frac{F}{c} \tag{23}$$

Then, the OCT provides the Euler-Lagrange equations for the adjoint variables

$$\frac{\mathrm{d}\lambda_r}{\mathrm{d}t} = -\frac{\mathrm{d}H}{\mathrm{d}r} \quad \frac{\mathrm{d}\lambda_v}{\mathrm{d}t} = -\frac{\mathrm{d}H}{\mathrm{d}v} \quad \frac{\mathrm{d}\lambda_m}{\mathrm{d}t} = -\frac{\mathrm{d}H}{\mathrm{d}m} \tag{24}$$

In the present work, the thrust is vertical during phase 1), parallel to the relative velocity during

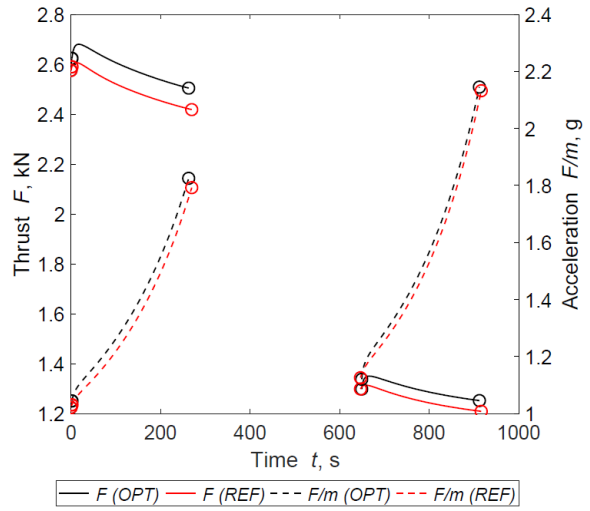

Fig. 3 Thrust F and acceleration F/m histories of the optimal solutions

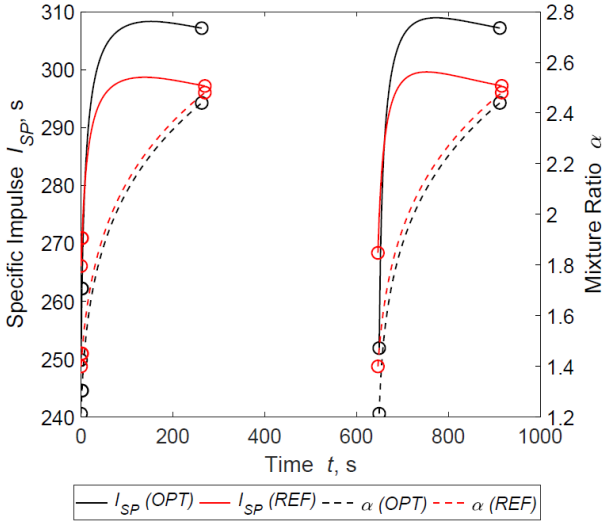

Fig. 4 Specific impulse I_{SP} and mixture ratio α histories of the optimal solutions

phase 2) and free and optimized during phase 4). Obviously thrust is zero during the coasting, i.e., during phase 3). The OCT provides the thrust during phase 4), which results to be parallel to the velocity adjoint vector, also known as the primer vector. Moreover, the OCT also gives the boundary conditions for optimality at the initial and final points, and at the boundaries of each phase (Casalino *et al*. 1999). The velocity adjoint vector has to be parallel to the velocity vector just after the velocity turn. The transversality conditions are also provided by the OCT, and relevant times can be determined. In this formulation, time is formally free, because mass constraints replace time boundaries. In the end, the application of the OCT leads to a multi-point boundary value problem, which is solved by an iterative procedure based on Newton's method (Colasurdo and Pastrone 1994).

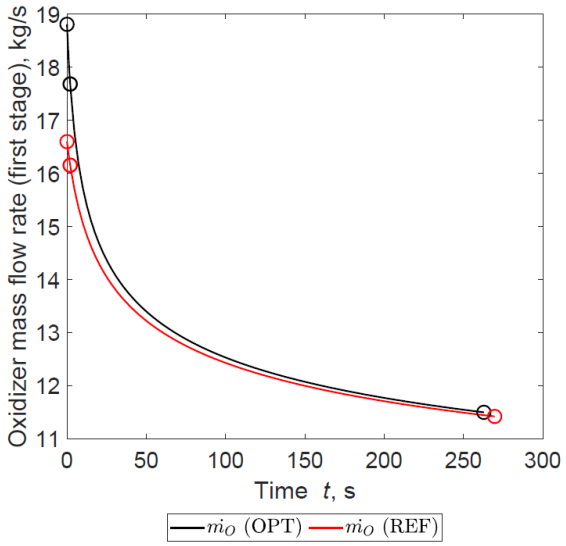

Fig. 5 Oxidizer mass flow rate during the first stage burn

Table 1 Overall MAV mass budget and performance

Case	μ	m_p	m_{dry}	α_{avg}	$I_{sp_{avg}}$	V_{losses}
-	kg	kg	kg	-	s	km s $^{-1}$
OPT	94.58	341.94	63.48	2.073	294.2	0.640
REF	93.04	348.78	58.18	2.128	290.9	0.665

Table 2 Hybrid engine design. The sixth column (m_e) reports the sum of electrical components masses (motor, pump and batteries)

Case	α_i	$(p_d)_i$	F_i	m_e	δ_{bp}	δ_{be}	E	d	L_{cc}	L_t	L_n
-	-	bar	kN	kg	kW kg $^{-1}$	Wh kg $^{-1}$	-	m	m	m	m
OPT	1.21	45.3	2.50	8.52	2.45	103.3	36.5	0.29	0.67	1.15	0.42
REF	1.40	22.7	2.50	2.93	6.95	198.5	18.8	0.30	0.66	1.14	0.40

5. Conclusions

In the present paper, the initial mass of the MAV is equal to 500 kg and the payload is expected to fall in the range between 75 kg and 100 kg. A 170-km circular equatorial orbit is considered, in the context of the Mars Sample Return Mission. The design variables, performance and mass budget for the optimal solution obtained by means of the proposed approach are reported as OPT in Table 1 and Table 2. On the other hand, the values reported as REF in the aforementioned Tables are taken from a different work on the same topic for the sake of comparison (Casalino *et al.* 2021c). Those results have been obtained regarding δ_{bp} and δ_{be} as constants, assuming their values before trajectory optimization (i.e., $t_b \neq t^*$), simply picking the highest values available in the literature (Kwak *et al.* 2018). In fact, one can notice that the REF case employs δ_{bp} and δ_{be} values which are roughly three times and twice the ones obtained in the OPT case, respectively,

Table 3 Design space survey: Optimized solutions

Case	α_i	$(p_d)_i$	E	μ
-	-	bar	-	kg
OPT	1.21	45.3	36.5	94.58
OPT $_1$	1.50	30.0	30.0	92.43
OPT $_2$	1.50	20.0	30.0	92.07
OPT $_3$	1.50	40.0	45.0	91.69
OPT $_4$	1.50	40.0	30.0	91.60
OPT $_5$	1.50	30.0	45.0	91.55

resulting in a relevant dry mass m_{dry} reduction (about 9 % of the REF case dry mass). Figures 3 and 4 depict the time history of the key performance index of the launcher. Looking at the thrust history right after the liftoff, one can notice that the OPT solution exhibits a greater increase in the thrust level with respect to the REF solution. This behavior is due to the higher nozzle expansion area ratio (36.5 vs. 18.8), despite the equal F_i, which is fixed to 2.5 kN for each engine in both the analysis. For the same reason, the thrust level of the OPT solution is slightly higher than the REF one throughout the second stage burn. Concerning the mixture ratio values, the OPT solution is characterized by both a lower initial and average value, which are able to grant a slight increase in the specific impulse value, which in turn leads to a smaller propellant mass m_p required for the mission. Such reduction in m_p is able to offset the increase of m_{dry} due to the lower electrical properties of the OPT case, resulting in a greater launcher payload mass μ (+1.5 kg). In the end, in Fig. 5 is depicted the oxidizer mass flow rate $\dot{m}_O$ during the first stage burn. $\dot{m}_O$ varies during hybrid engine operation, despite the assumption of a constant power level for the pump, in accordance to Eq. (4) and Eq. (11). The behavior of $\dot{m}_O$ is analogous during second stage burn, and is here omitted to be brief.

In the end, looking at the values of E and L_n reported in Table 2, one can notice a far larger value of E for the OPT solution, but an almost unchanged value of L_n. The choice of E is viable because the greater initial discharge pressure $(p_d)_i$ of the OPT case leads to a far smaller nozzle throat area, in order to have the same initial thrust F_i (which is fixed in both the approaches). Hence, a larger value of the nozzle expansion area ratio can be employed, contributing to the aforementioned benefits in terms of specific impulse without an excessive increase in nozzle and engine dry mass.

The author performed survey of the design space to ensure that the OPT solution represents a global optimum. The following ranges were used in the survey for the engine design parameters: $1 \leq \alpha_i \leq 3$, $20 \leq E \leq 50$ and $15 \text{ bar} \leq (p_d)_i \leq 60$ bar. The design space was discretized by means of an equally spaced grid. The five best solutions are reported in Table 3 as OPT $_i$, with $1 \leq i \leq 5$. All the OPT $_i$ solutions exhibited a level of performance lower than the solution found out by the coupled optimization procedure, thus the OPT solution can be regarded as a global optimum, at least inside the design space surveyed.

These results show that the proposed approach for the optimal selection of the battery characteristic, embedded into the coupled engine/trajectory optimization, is able to offset the technological gap between the commercial lithium battery considered here and the advanced ones employed in (Casalino *et al*. 2021c). In fact, looking at Table 1, one can notice that the payload mass μ of the OPT case is even slightly greater than the REF one. Further performance

improvements, in terms of delivered payload, may be achieved once the correlations for t^* and δ_{be} for the most recent and aerospace-grade batteries are provided.

References

Barker, D.H., Belnap, R.D., Hall, A.F. and Kordig, J.W. (1965). "A simplified method of predicting char formation in ablating rocket exit cones (Char formation in solid rocket nozzle exit cones made from reinforced plastic predicted from corrosion standpoint)", *Chem. Eng. Prog., Symposium Ser.*, **61**(59), 108-11.

Barrere, M., Jaumotte, A., Fraeijs de Veubeke, B. and Vandenkerckhove, J. (1960), *Rocket Propulsion*, Rapport du LTAS, Elsevier Publishing Company.

Boiron, A.J. and Cantwell, B. (2013), "Hybrid rocket propulsion and in-situ propellant production for future mars missions", *49th AIAA/ASME/SAE/ASEE Joint Propulsion Conference*, San Jose, CA, July.

Casalino, L. and Pastrone, D. (1994), "Indirect optimization method for impulsive transfers", *Astrodynamics Conference*, Scottsdale, AZ, August.

Casalino, L. and Pastrone, D. (2005a), "Optimal design and control of hybrid rockets for access to space", *41st AIAA/ASME/SAE/ASEE Joint Propulsion Conference and Exhibit*, Tucson, AR, July.

Casalino, L. and Pastrone, D. (2005b), "Oxidizer control and optimal design of hybrid rockets for small satellites", *J. Propuls. Power*, **21**(2), 230-238. https://doi.org/10.2514/1.6556.

Casalino, L. and Pastrone, D. (2010a), "Optimal design of hybrid rocket motors for launchers upper stages", *J. Propuls. Power*, **26**(3), 421-427. https://doi.org/10.2514/1.41856.

Casalino, L. and Pastrone, D. (2010b), "Optimization of a hybrid rocket upper stage with electric pump feed system", *46th AIAA/ASME/SAE/ASEE Joint Propulsion Conference & Exhibit*, Nashville, TN, July.

Casalino, L. and Pastrone, D. (2012), "Optimization of hybrid sounding rockets for hypersonic testing", *J. Propuls. Power*, **28**(2), 405-411. https://doi.org/10.2514/1.B34218.

Casalino, L. and Pastrone, D. (2014), "Optimization of hybrid propellant mars ascent vehicle", *50th AIAA/ASME/SAE/ASEE Joint Propulsion Conference*, Cleveland, OH, July.

Casalino, L., Colasurdo, G. and Pastrone, D. (1999), "Optimal low-thrust escape trajectories using gravity assist", *J. Guid., Control Dyn.*, **22**(5), 637-642. https://doi.org/10.2514/2.4451.

Casalino, L., Letizia, F. and Pastrone, D. (2012), "Design trade-offs for hybrid rocket motors", *48th AIAA/ASME/SAE/ASEE Joint Propulsion Conference & Exhibit*, 4202.

Casalino, L., Masseni, F. and Pastrone, D. (2019), "Viability of an electrically driven pump-fed hybrid rocket for small launcher upper stages", *Aerosp.*, **6**(3), 36. https://doi.org/10.3390/aerospace6030036.

Casalino, L., Masseni, F. and Pastrone, D. (2019o), "Robust design approaches for hybrid rocket upper stage", *J. Aerosp. Eng.*, **32**(6), 04019087. https://doi.org/10.1061/(ASCE)AS.1943-5525.0001078.

Casalino, L., Masseni, F. and Pastrone, D. (2021a), "Deterministic and robust optimization of hybrid rocket engines for small satellite launchers", *J. Spacecraft Rocket.*, **58**(6), 1893-1903. https://doi.org/10.2514/1.A35007.

Casalino, L., Masseni, F. and Pastrone, D. (2021b), "Hybrid rocket engine design optimization at Politecnico di Torino: A review", *Aerosp.*, **8**(8), 226. https://doi.org/10.3390/aerospace8080226.

Casalino, L., Masseni, F. and Pastrone, D. (2021c), "Optimal design of electrically-fed hybrid mars ascent vehicle", *Aerosp*., **8**(7), 181. https://doi.org/10.3390/aerospace8070181.

Evans, B. and Cantwell, B. (2019), "Development and testing of Sp7 fuel for mars ascent vehicle application", *2019 IEEE Aerospace Conference*, Yellowstone, MN, March.

Funami, Y. (2019), "Two-dimensional fuel regression simulations with level set method for hybrid rocket internal ballistics", *Adv. Aircraft Spacecraft Sci.*, **6**(4), 333-348. https://doi.org/10.12989/aas.2019.6.4.333.

Kamps, L., Hirai, S. and Nagata, H. (2021), "Hybrid rockets as post-boost stages and kick motors", *Aerosp.*, **8**(9), 253. https://doi.org/10.3390/aerospace8090253.

Karabeyoglu, M.A., Altman, D. and Cantwell, B.J. (2002), "Combustion of liquefying hybrid propellants: Part 1, General theory", *J. Propuls. Power*, **18**(3), 610-620. https://doi.org/10.2514/2.5975.
Kwak, H.D., Kwon, S. and Choi, C.H. (2018), "Performance assessment of electrically driven pump-fed Lox/kerosene cycle rocket engine: Comparison with gas generator cycle", *Aerosp. Sci. Technol.*, **77**, 67-82. https://doi.org/10.1016/j.ast.2018.02.033.
McBride, B.J., Reno, M.A. and Gordon, S. (1994), "Cet93 and Cetpc: An interim updated version of the nasa lewis computer program for calculating complex chemical equilibria with applications", NASA TM-4557, NASA, Washington.
McCollum, L.T., Schnell, A., Yaghoubi, D., Bean, Q., McCauley, R. and Prince, A. (2019), "Development concepts for Mars Ascent Vehicle (MAV) solid and hybrid vehicle systems", *2019 IEEE Aerospace Conference*, Yellowstone, MN, March.
Muirhead, B.K. and Karp, A. (2019), "Mars sample return lander mission concepts", *2019 IEEE Aerospace Conference*, Yellowstone, MN, March.
Nagata, H., Nakayama, H., Watanabe, M., Wakita, M. and Totani, T. (2014), "Accuracy and applicable range of a reconstruction technique for hybrid rockets", *Adv. Aircraft Spacecraft Sci.*, **1**(3), 273. https://doi.org/10.12989/aas.2014.1.3.273.
Oglesby, B., Prince, A., Story, G. and Kam, A. (2019), "Qualification of a hybrid propulsion system for a mars ascent vehicle", *2019 IEEE Aerospace Conference*, Yellowstone, MN, March.
Price, H., Cramer, K., Doudrick, S., Lee, W., Matijevic, J., Weinstein, S., ... & Mitcheltree, R. (2000), "Mars sample return spacecraft systems architecture", *2000 IEEE Aerospace Conference. Proceedings*, **7**, 357-375.
Saito, Y., Yokoi, T., Neumann, L., Yasukochi, H., Soeda, K., Totani, T., ... & Nagata, H. (2017), "Investigation of axial-injection end-burning hybrid rocket motor regression", *Adv. Aircraft Spacecraft Sci.*, **4**(3), 281. https://doi.org/10.12989/aas.2017.4.3.281.
Shotwell, R., Benito, J., Karp, A. and Dankanich, J. (2016), "Drivers, developments and options under consideration for a mars ascent vehicle", *2016 IEEE Aerospace Conference*, Yellowstone, MN, March.
Sutton, G.P. and Biblarz, O. (2001), *Rocket Propulsion Elements*, John Wiley & Sons.

Nomenclature

A_b	burning surface area, m ^{2}
A_p	port area, m ^{2}
A_{th}	nozzle throat area, m ^{2}
a	regression constant, m $^{1+2n}$ kg $^{-n}$ s $^{n-1}$
C_F	thrust coefficient
c^*	characteristic velocity, m/s
D	drag vector, N
d	rocket outer diameter, m
F	thrust vector, N
F	thrust, N
G	gravitational constant, Nm ^{2}/kg ^{2}
g	gravity acceleration, m/s ^{2}
H	Hamiltonian
h	altitude, km
I_{SP}	mean specific impulse, s
J	throat area to initial port area ratio
L	overall engine length, m

L_b	fuel grain length, m
$M_{♂}$	Mars mass, kg
m	mass, kg
N	number
n	mass-flux exponent
P_e	electric power, kW
p	pressure, bar
r	position vector, m
t	time, s
T	temperature, K
v	velocity vector, m/s
w	web thickness, m
y	burning distance, m
Z	hydraulic resistance, 1/(kg m)
α	mixture ratio
γ	specific heat ratio
δ_{ep}	electric motor and pump power density, kW/kg
δ_{be}	batteries energy density, Wh/kg
δ_{bp}	batteries power density, kW/kg
E	nozzle area ratio
η_{ep}	electric motor and pump efficiency
λ	adjoint variable
μ	payload, kg
ρ	density, kg/m ^{3}

Superscripts

$\dot{}$	time derivative
$*$	characteristic

Subscripts

1	combustion chamber at head-end
atm	atmospheric
avg	average
cc	combustion chamber
d	discharge
dry	dry
e	nozzle exit
ep	electric motor and pump
F	fuel
f	final value
i	initial value

n	nozzle
O	oxidizer
p	overall propellant (oxidizer + fuel)
rel	relative
t	oxidizer propellant tank
th	throat
tot	total
vac	vacuum